

Molecular-dynamics simulation of methane-hydrate crystallisation in terahertz electromagnetic fields: Assessment of field intensities

Niall J. English

Citation: Chin. Phys. B, 2026, 35 (**5**): 050501. DOI: 10.1088/1674-1056/ae5474
http://cpb.iphy.ac.cn; http://iopscience.iop.org/cpb

What follows is a list of articles you may be interested in

Spiral trajectories of asymmetric molecules

Nan Sheng(盛楠), Shiqi Sheng(盛世奇), Yu-Song Tu(涂育松), Rong-Zheng Wan(万荣正), Zuo-Wei Wang(王作维), Zhanchun Tu(涂展春), and Hai-Ping Fang(方海平)
Chin. Phys. B, 2025, 34 (**8**): 080507. DOI: 10.1088/1674-1056/adcea0

Stable water droplets on composite structures formed by embedded water into fully hydroxylated *β*-cristobalite silica

Hanqi Gong(龚菡琪), Chonghai Qi(齐崇海), Junwei Yang(杨俊伟), Jige Chen(陈济舸), Xiaoling Lei(雷晓玲), Liang Zhao(赵亮), and Chunlei Wang(王春雷)
Chin. Phys. B, 2021, 30 (**1**): 010503. DOI: 10.1088/1674-1056/abc2b7

Active Brownian particles simulated in molecular dynamics

Liya Wang(王丽雅), Xinpeng Xu(徐新鹏), Zhigang Li(李志刚), Tiezheng Qian(钱铁铮)
Chin. Phys. B, 2020, 29 (**9**): 090501. DOI: 10.1088/1674-1056/aba60d

Fast and accurate determination of phase transition temperature via individual generalized canonical ensemble simulation

Ming-Zhe Shao(邵明哲), Yan-Ting Wang(王延颋), Xin Zhou(周昕)
Chin. Phys. B, 2020, 29 (**8**): 080505. DOI: 10.1088/1674-1056/ab9c03

One-dimensional mass transport with dynamic external potentials

Xingxing Zhang(张星星), Dongqin Zheng(郑冬琴), Weirong Zhong(钟伟荣)
Chin. Phys. B, 2019, 28 (**2**): 020505. DOI: 10.1088/1674-1056/28/2/020505

SPECIAL TOPIC — John Tse: Pioneer in high-pressure materials science

Molecular-dynamics simulation of methane-hydrate crystallisation in terahertz electromagnetic fields: Assessment of field intensities

Niall J. English[†]

School of Chemical and Bioprocess Engineering, University College Dublin, Belfield, Dublin 4, *Ireland*

(Received 6 January 2026; revised manuscript received 9 March 2026; accepted manuscript online 19 March 2026)

Non-equilibrium molecular dynamics simulations were conducted to study the growth and dissolution of a spherical methane hydrate crystallite, using a polarizable water potential, encircled by a liquid phase of saturated water and methane, both in the microwave to far-infrared range and under applied external electromagnetic (e/m) fields (5 GHz to 7.5 THz) at r.m.s. electric-field strengths of up to the order of 1 V·nm^{-1} — in an attempt to assess and model the "threshold" field intensities required to initiate hydrate dissolution. The average growth rate of the crystallite in the absence of a field was found to be approximately 0.32 water and 0.045 methane molecules per picosecond. Upon applying e/m fields, deviations from zero-field crystal growth patterns were observed for r.m.s. field strengths, especially at $\sim$ 1 V·nm^{-1} as a rough 'threshold'. When the water dipole was aligned with the external field, systematic frequency variations were observed, providing a mechanistic rationale for field-coupling effects on dipole direction/magnitude and hydrogen-bonding shifts.

Keywords: molecular dynamics, clathrate hydrates, crystallisation, electromagnetic fields

PACS: 05.10.–a

DOI: 10.1088/1674-1056/ae5474 **CSTR:** 32038.14.CPB.ae5474

1. Introduction

Water molecules form a host lattice that creates cavities for the tiny guest atoms or molecules — to form a crystalline inclusion compound — known as clathrate hydrates. Methane hydrates, which usually have the sI-polymorph structure, are the most prevalent *in-situ* hydrates found in nature. They can be found in permafrost and marine-sediment environs. The potential of methane clathrates as a novel source of natural gas has led to a significant increase in global interest in these materials in recent years.[1–5] The global interest in this topic has spurred a variety of molecular dynamics simulations, many of which investigate methane-hydrate extraction techniques, typically from marine-sediment environments. Overall, molecular simulation has been very helpful in clarifying many of the fundamental equilibrium characteristics of gas hydrates, such as their structure,[6–10] phonon "resonant-scattering" by guest molecules in cages,[11,12] hydrogen-bonding behaviour,[12] and dynamical and energetic properties.[10,13] Molecular dynamics (MD) has greatly advanced our understanding of equilibrium phonon scattering and time-dependent properties, which has resulted in many advances, especially in understanding the underlying thermal-conduction mechanisms in clathrates,[11,12] as well as guest diffusion based on "cage-hopping", which is relevant to energy and gas-storage applications.[13] Hydrate-formation kinetics are still not well understood,[2,13] despite dramatic recent advancements in simulation-facilitated comprehension of clathrate-equilibrium properties. Nucleation and crystallization of hydrates have been studied through a number of molecular-simulation studies.[2,13]

A significant number of technical issues within the oil and gas-processing industries are rooted in the desire to both promote and prevent the formation of natural gas hydrates. For example, hydrate nucleation, agglomeration, and growth are inhibited by the injection of chemicals, such as methanol and various glycols, into gas streams. While greater clarity exists than for nucleation, the precise molecular-scale mechanisms underlying hydrate growth are still unknown. Although the limited timescales amenable to MD and the mass transfer of guest molecules are undoubtedly important factors, a less explored area in the inhibition of hydrate nucleation and formation lies in the use of electromagnetic fields. Exposing hydrate-fluid systems to external electromagnetic fields at suitable intensities and frequencies represents a potentially desirable approach with practical and cost-effective options. Rojey[14] has filed a U.S. patent on a method that exposes pipeline systems to a field of pulsed electromagnetic waves created by a network of emitters spaced along the pipeline's length in order to inhibit or prevent the formation of clathrate hydrates. In essence,[14] e/m waves with frequencies between 1 GHz and 300 GHz, particularly in the 1 GHz to 10 GHz range, are expected to hinder or prevent the arrangement of water molecules into a hydrogen-bonded crystalline lattice,

[†]Corresponding author. E-mail: niall.english@ucd.ie

© 2026 Chinese Physical Society and IOP Publishing Ltd. All rights, including for text and data mining, AI training, and similar technologies, are reserved.

thereby disrupting hydrate growth.

This is undoubtedly more appealing than the highly expensive downstream "cleaning" process of extracting inhibitors. In his analysis of the impact of electric fields on hydrate crystals, Makogon developed an expression for the change in thermodynamic equilibrium conditions caused by a stationary electric or magnetic field. He concluded that the intensity of the electric field would need to be on the order of 10^8 V/m (i.e., 0.1 V·nm^{-1}) to have any discernible impact on equilibrium. A model for the e/m field-induced melting of hydrate deposits in porous rock wells was also described by Makogon.[1] For gas pipeline flow assurance, external electric fields would therefore serve as a substitute for the more conventional methods of applying additives.[1] Although e/m-field penetration depths in liquid water are only a few centimetres, they can reach up to metres in gas.[14] This, along with repeated specular reflection along the pipe walls (in a "zig-zag" fashion), helps to maintain relatively high amplitude over hundreds of metres. For this reason, new field emitters are specified in Rojey's patent every few hundred meters of pipeline. Unfortunately, little industrial R&D has been conducted in the last 20 years regarding these electric-field methods for gas-hydrate applications, and virtually no developmental work has been reported in the open literature. Our motivation to investigate additional electric-field effects on hydrates stems from this intriguing flow-assurance proposition's relative neglect. To determine how external e/m fields affect the formation of spherical methane-hydrate nano-crystallites, English and MacElroy conducted non-equilibrium MD.[15] They discovered that the structural hydrogen-bonding arrangements within the crystallite are weakened by shifting dipolar alignment, which causes break-up (or inhibits formation initially). This effect depends on the frequency and intensity of the field; to observe inhibition within realistic MD simulation times, intensities of 0.1–0.5 V·nm^{-1} are required. The range of 0.02–0.2 THz, which overlaps with the average hydrogen-bond lifetimes, was the "optimal" frequency range for disruption. This partially validates the claims made by Rojey.[14,15] Specifically, e/m fields larger than approximately 1 V·nm^{-1} in root-mean-square (r.m.s.) intensity led to the "electro-dissociation" of hydrate nano-crystals, with the 50–100 GHz band showing the fastest results. Even at r.m.s. intensities close to 2 V·nm^{-1}, however, more recent non-equilibrium MD studies on bulk methane clathrates showed that external e/m fields do not cause "electro-dissociation" at least within nanosecond time intervals.[16] Luis and others found that when static electric fields larger than 1.5 V·nm^{-1} were applied to bulk methane hydrate instead of spherical nanocrystals, the methane hydrate destabilized at 248 K and 2 MPa.[17–19]

The current work is predicated on the electro-dissociation research of references 15 to 19 and on Rojey's patent.[14] It was believed that applying e/m fields at the appropriate frequency and intensity would modify the solid-liquid hydrate system's hydrogen-bonding configurations, which would subsequently impact the rate of crystallization. Examining these field effects on crystallization and determining the intensity range that best prevents hydrate growth are the main driving forces behind this work — especially for lower-intensity cases below the "electro-dissociation" threshold of $\sim$ 1 V·nm^{-1}.

2. Methodology

The reader is referred to Ref. [15] for more information about the system setup. In a similar fashion, the present work created a variety of non-equilibrium two-phase systems to initiate crystal-growth MD simulations. This was done by using roughly spherical methane-hydrate nano-crystallites with radii between 9 Å and 12.5 Å to seed a methane-supersaturated aqueous liquid phase. In the current work, the majority of the analysis is concentrated on the larger, $\sim$ 12.5 Å cases because Ref. [15] indicates that these are more clearly in the realm of outright crystal-growth régime, well beyond the critical radius.

Regarding possible concerns that periodically replicating crystallite images in neighboring periodically imaged boxes could impede growth, the size of the cubic simulation box was determined to be approximately 42 Å.[15] At no point do the grown crystals in the current study nearly fill the simulation box, which would be expected to contribute to artificially accelerated crystallization kinetics.[2,15]

The ensuing 2288-molecule system with the 12.5 Å-radius crystallite contained 1949 water and 339 methane molecules, while the 2275-molecule system with the 9 Å-radius core contained 1944 water and 331 methane molecules.[15] Three 2288-molecule systems with varying degrees of initial NVT relaxation were constructed and designated as "1", "2", and "3".[15] An NPT-based MD relaxation to 220 K and 600 bar was performed on these systems, and no appreciable changes were observed in the crystal cores' size, structure, or identity. Regarding the three 12.5 Å crystallites, these nano-clusters were extremely similar.[15]

Table 1. Potential parameters used in the methane model.

	Rigid	Flexible
ε_{CC} (kcal/mol)	0.326	0.1094
σ_{CC} (Å)	3.64	3.8164
ε_{HH} (kcal/mol)		0.0157
σ_{HH} (Å)		2.9744
θ_{HCH} (degrees)	109.5	
r_{CH} (Å)	1.09	
Q_H (e)	0.14	0.116

The current study used a five-site rigid methane model comprised of partial charges on the carbon and hydrogen

atoms, as well as the rigid/polarizable TIP4P-FQ water potential[20] and a Lennard–Jones (LJ) 12–6 interaction site on the carbon atom. The potential-model parameters for the methane are given in Table 1.

The TIP4P-FQ model is a molecular dynamics model for water that uses the TIP4P geometry,[20] in conjunction with dynamic transfer of charge between atomic sites based on the principle of electronegativity equalization.

Using a second-order expansion for the energy required to create a partial charge in an isolated atom, Ref. [20] expressed the energy of a system of N_{mol} molecules, each composed of N_{atom} atoms, as

$$\begin{aligned} U(\boldsymbol{Q},\boldsymbol{r}) = & \sum_{i=1}^{N_{\mathrm{mol}}}\sum_{a=1}^{N_{\mathrm{atom}}}\left[\chi_a^0 Q_{ia} + \frac{1}{2}\sum_{b=1}^{N_{\mathrm{atom}}} Q_{ia}Q_{ib}J_{ab}(r_{ia,ib})\right] \\ & + \sum_{ia<jb} J_{ab}(r_{ia,jb})Q_{ia}Q_{jb} \\ & + \sum_{ia<jb} V(r_{ia,jb}) - N_{\mathrm{mol}}E_{\mathrm{gp}}, \end{aligned} \tag{1}$$

where χ_a^0 represents the Mulliken electronegativity (per electronic charge e) of atom a, and J_{aa}^0 is twice the hardness of the electronegativity of the isolated atom. $J_{ab}(r_{ia,jb})$ is the Coulombic interaction, and V is any additional non-Coulombic interaction between the atomic sites ia and jb. E_{gp} is the gas-phase energy that must be subtracted (since the total energy is defined relative to the isolated gas-phase energy). The electronegativity per unit charge of atom a is given by

$$\chi_a = \frac{\partial U}{\partial Q_a}. \tag{2}$$

The charges Q_{ia}, by the principle of electronegativity equalization, are those for which the electronegativities χ_{ia} are equal, which is equivalent to minimizing the energy, subject to the constraint that each molecule is electroneutral.

The gas-phase energy E_{gp} is determined by considering the charge that minimizes the energy of an isolated gas-phase water molecule, and Ref. [20] shows this for TIP4P-FQ water

$$E_{\mathrm{gp}} = \frac{-(\chi_{\mathrm{O}}^0 - \chi_{\mathrm{H}}^0)^2}{2J_{\mathrm{OO}}^0 + J_{\mathrm{HH}}^0 - 4J_{\mathrm{OH}}(r_{\mathrm{MH}}) + J_{\mathrm{HH}}(r_{\mathrm{HH}})}. \tag{3}$$

The Coulombic interaction $J_{ab}(r_{ia,jb})$ for intramolecular interactions is defined as the Coulomb overlap integral between the Slater atomic orbitals centered on each site, while the intermolecular interaction is defined as the pure Coulomb interaction $1/r$, which is implemented in this work using the Lekner method. The intramolecular interaction J_{ij} is characterized by the parameters ζ_{O} and ζ_{H}, and use of the parameters in Ref. [20] allows evaluation of J_{OO}, J_{OH}, J_{HH}, $\partial J_{\mathrm{OH}}/\partial r$, and $\partial J_{\mathrm{HH}}/\partial r$ at the separations required by the TIP4P geometry. This is shown in Table 2.

Table 2. Results for overlap integrals and derivatives of TIP4P-FQ model.

ζ_{O} (a_0^{-1})	1.63
ζ_{H} (a_0^{-1})	0.90
J_{OO}^0 (kcal/(mol·e^2))	371.6
J_{HH}^0 (kcal/(mol·e^2))	353.0
$J_{\mathrm{OH}}(r_{\mathrm{MH}})$ (kcal/(mol·e^2)), where $r_{\mathrm{MH}} = 0.873$ Å	286.4
$J_{\mathrm{HH}}(r_{\mathrm{HH}})$ (kcal/(mol·e^2)), where $r_{\mathrm{HH}} = 1.514$ Å	203.6
$\mathrm{d}J_{\mathrm{OH}}(r_{\mathrm{MH}})/\mathrm{d}r$ (kcal/(mol·e^2·Å))	−163.9
$\mathrm{d}J_{\mathrm{HH}}(r_{\mathrm{HH}})/\mathrm{d}r$ (kcal/(mol·e^2·Å))	−99.45

These models performed well in comparison to systems that used flexible and non-polarizable water models for the simulation of hydrates and water, which is why they were selected for the crystal-growth investigations.[15] Using the previously mentioned interpolation scheme, the Lekner method was applied to handle long-range electrostatic interactions.[21–24] For interactions between various kinds of LJ sites, the Lorentz–Berthelot mixing rules were applied, and the cut-off radius for LJ interactions was set at 10 Å. Reference [15] outlines the application of the Báez–Clancy hydrate-recognition criteria.

In Ref. [15], the water-methane systems were subjected to a succession of pure electric fields, as previously mentioned. The fields had frequencies ranging from 5 GHz, 35 GHz, and 40 GHz to 7.5 THz and r.m.s. electric-field intensities between 0 and 2 V·nm^{-1}. Given the continuous nature of the water's experimental spectrum, the e/m absorption process in the liquid state can be treated using classical mechanics.[25,26] The infrared spectra of other types of hydrate are continuous, despite the lack of reported experimental spectra for methane hydrate.[27,28] High-intensity fields were used to observe the non-thermal effect of dipole alignment and to test the potential models to an extreme degree by enabling the observation of significant molecular rotations. This group of simulations, which will henceforth be referred to as non-equilibrium NPT (NNPT) simulations, was used in conjunction with the NPT ensemble (which had a set temperature and pressure of 220 K and 600 bar) to isolate the physical field effects at constant temperature. NNPT simulations are useful for evaluating non-thermal field effects.[15]

A 1.5–15 fs timestep was used, in conjunction with a TIP4P-FQ charge mass of 15×10^{-5} (ps/e)^2 kcal/mol. For NPT dynamics, τ_{Q} and τ_{B} were set at 100 fs and 500 fs, respectively. τ_{Q} was set to 50 fs for the control of the TIP4P-FQ electronic temperature, with the set value at 1 K.

3. Results and discussion

Considering that crystal formation was noted in Ref. [15] under zero-field conditions at a temperature and pressure of 220 K and 600 bar, these parameters were chosen for the simulations in this investigation. Every simulation lasted 0.5 ns,

during which noticeable growth was observed on the "scaffolds" of the nanoclusters. Figure 1 displays the number of hydrate-like water molecules for each of the three crystals in the 2288-molecule systems as determined by the NPT simulations, while figure 2 displays the same information for the 2275-molecule system in the NPT ensemble. The size-time data were fitted with a straight-line regression following an initial phase of enhanced crystal formation lasting approximately 30 ps. Strictly, crystallization is a non-linear process, and straight-line fits act as mere guides to the eye. Figures 1 and 2 show that the crystal size fluctuates rapidly for brief periods around an average value. The quick growth seen in the first 30 ps to 40 ps is transient and related to the water molecules' rotational relaxation at the interface. Subsequent crystal formation occurs more slowly and exhibits larger size fluctuations. The initial transient does not influence growth rates to any substantial extent, as these growth rates were estimated from post-transient data. It was discovered that the crystallite grew at an average rate of about 0.32 water and 0.045 methane molecules per picosecond. The growth process can be better understood by using computer graphics to visualize hydrate configurations over time. Figure 3 shows snapshots of hydrate clusters for the 9 Å crystallite at various stages of the simulation. Fluctuations in hydrate-phase classification during the simulations cause variations in the cluster sizes and structures in the snapshots. The freshly bonded hydrate structures exhibited some deformation compared to the initial nanocrystal template. The stabilization of the hydrate cavities depends on the diffusion of methane and water molecules. Individual cages are completed and consolidated to produce growth.

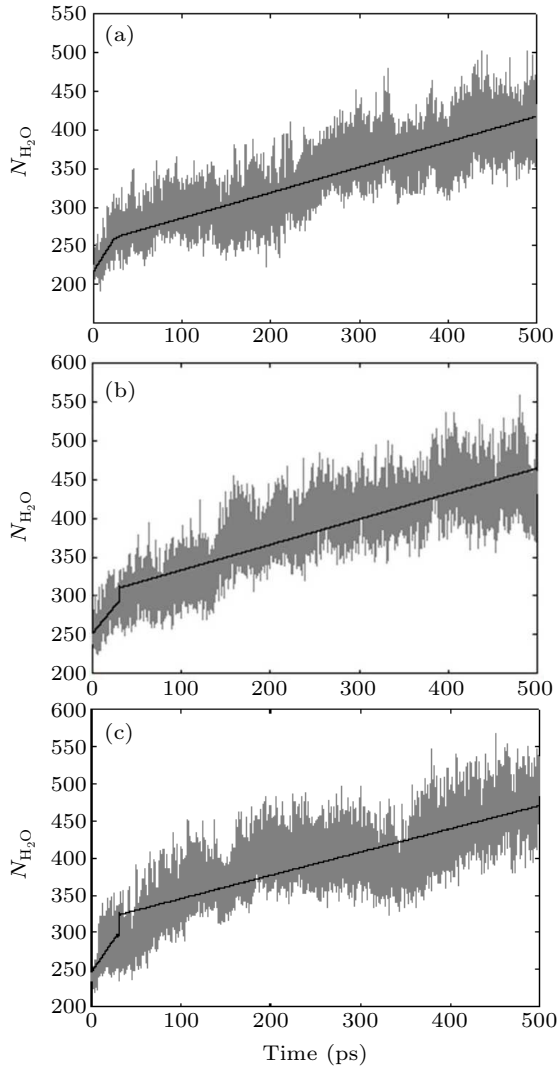


Fig. 1. Hydrate-cluster size as a function of time for the 2288-molecule system in the NPT ensemble for systems (a) 1, (b) 2, and (c) 3.

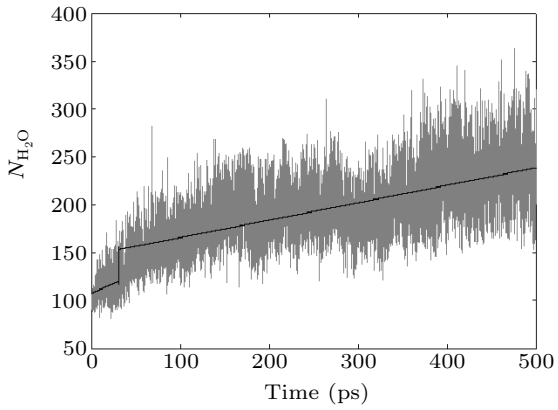


Fig. 2. Hydrate-cluster size as a function of time for the 2275-molecule system in the NPT ensemble.

Following the initial transient phase of molecular realignment at the interface, the NPT size-time results for the three systems containing 2288 molecules each show comparable crystal growth rates. On systems 2 and 3, however, the cluster size-time data clearly show the effects of NVT melting. The number of enclathrated water molecules affects reorientational relaxation during the first phase, indicating variations between the systems.

Radial distribution functions (RDFs) for water–water site–site interactions are shown in Fig. 4 at different points during the crystallization process, averaged for the systems containing crystallites with a radius of 12.5 Å. The times of 2 ps, 6 ps, 58 ps, and 500 ps correspond to the centres of the four-period sampling windows used to compute the RDFs. As time progresses, it is evident that the peak structure in the water–water RDFs becomes more prominent; that is, the principal and secondary peaks increase in height, and the troughs' depths also increase correspondingly. As water molecules are incorporated onto the initial nanocrystal template, the number of hydrogen bonds in the system increases, as illustrated using the 9 Å-radius crystallite as an example. Given the larger differences in RDF results at earlier times, it is easy to observe the early rapid crystal "growth" resulting from the reorientation of water molecules in the liquid phase at the interface. Therefore, the RDFs provide only a qualitative indicator of changes

in system structure induced by hydrate formation. This is expected, since 80–90% of the molecules in the system remain in the liquid state.

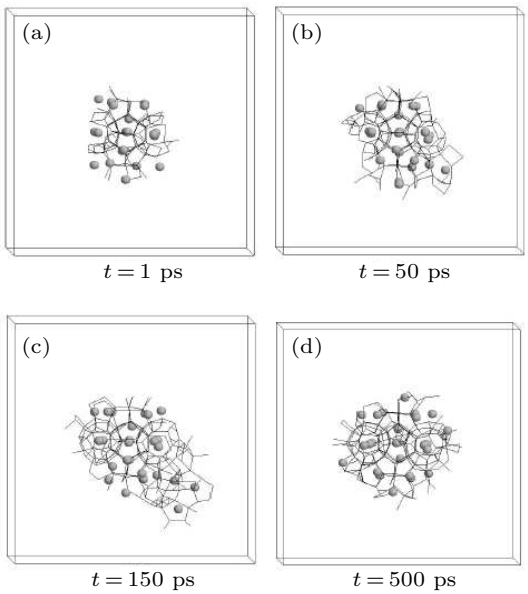


Fig. 3. Snapshots of the cluster configurations for the 9 Å nanocrystal.

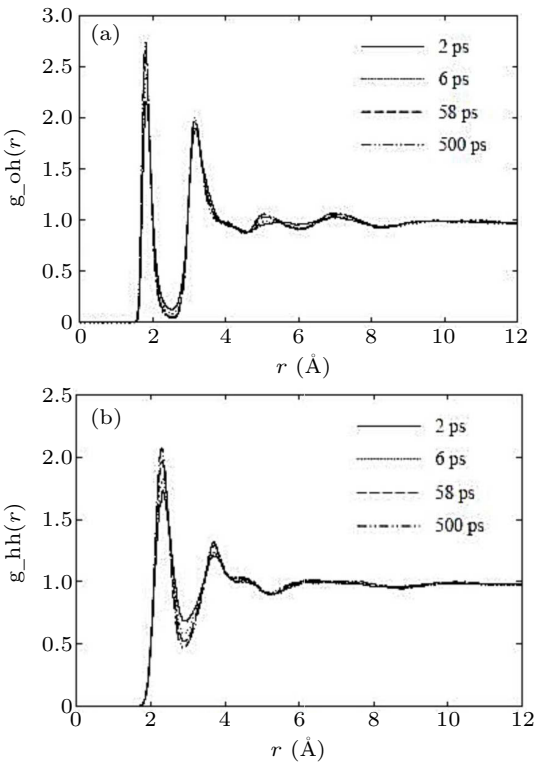


Fig. 4. Intermolecular (a) oxygen-hydrogen and (b) hydrogen-hydrogen PDFs between water molecules at various stages of NPT crystallisation simulation for the 2288-molecule system 1.

The trajectories of the total-system potential energy for the 2288-molecule systems 1 & 2, as well as for the 2275-molecule system (initially containing the smaller 9 Å crystallite), are depicted in Fig. 5(a). The corresponding water–water component[29,30] trajectories are shown in Fig. 5(b). A dramatic decrease in the system potential energy occurs during the early part of the simulation, corresponding to interfacial reorientational relaxation: the main energetic stabilization in the system's structure arises from the water–water distributions (as a consequence of relaxation), which mirrors the formation of hydrogen bonds (as visualized in Fig. 3 and also in the water–water "RDF sharpening" shown in Fig. 4). In Fig. 5, the results are similar for both crystallite sizes; thereafter, the rate of potential-energy stabilization is more modest, commensurate with the slower rate of hydrate formation.

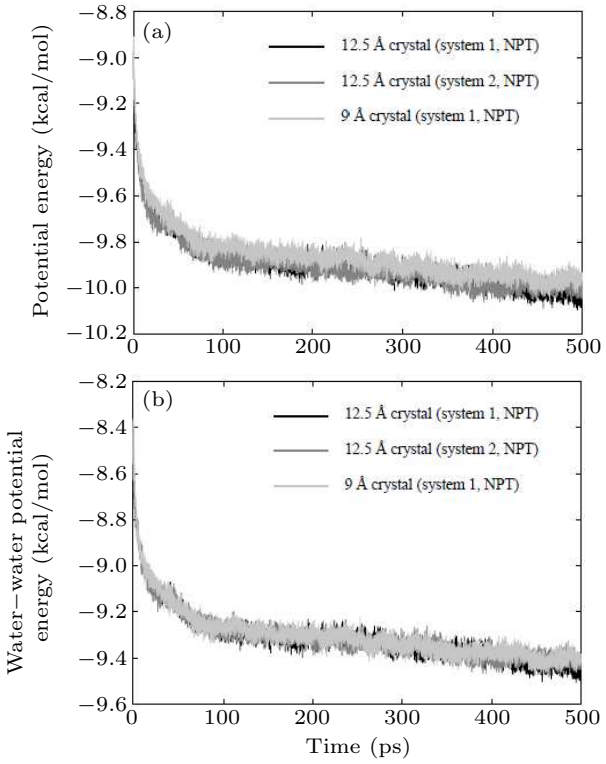


Fig. 5. (a) Total potential energy for zero-field crystallisation simulations 0. (b) Water–water potential energy for zero-field crystallisation simulations

Aside from the 2275-molecule system in the NPT ensemble (containing the smaller initial cluster), the time variation of the average molecular dipole moment of the water molecules is shown in Fig. 6, defined as the average of the dipoles of individual molecules, which fluctuate in time and space according to the electronegativity-equalisation paradigm.[20] This system contains a nanocrystal with an initial radius of approximately 12.5 Å. The increasing number of water molecules in the more energetically stable hydrate configuration raises the average dipole moment, arising from the greater separation of charge between the oxygen and hydrogen atoms. This results in a significant increase in the dipole moment, which rises from about 2.7 D to 2.82 D in the first 60 ps of the runs. As crystal formation progresses, the average molecular dipole moment continues to grow. As expected, the dipole moment is slightly smaller for the 2275-molecule system, where more molecules remain in the liquid phase.

The number of hydrogen bonds in the system, according to the Luzar–Chandler criteria, is illustrated in Fig. 7 for the same three systems. For the 1949 water molecules in the 2288-molecule system, a reasonable maximum number of hydrogen bonds is $1949 \times 2 = 3898$. Similarly, it would be 3888 hydrogen bonds for the 1944 water molecules in the 2275-molecule system. The number of hydrogen bonds increases from about 3500 to slightly over 3700 in the first 50 ps, as the water molecules near the interface relax and adopt orientational configurations closer to those of the hydrate state. It is apparent from the number of hydrogen bonds present, i.e., 3500 up to almost 3800, that the majority are still in the liquid phase. Nevertheless, the increase in the number of hydrogen bonds indicates hydrate formation. As with the average molecular dipole moment, the number of hydrogen bonds is marginally lower for the 2275-molecule system, containing the smaller initial hydrate cluster, as expected.

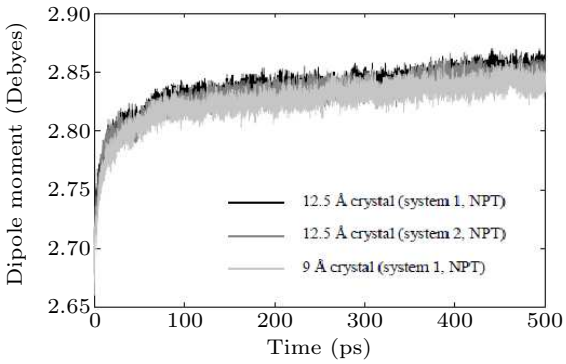


Fig. 6. Molecular dipole moment for zero-field crystallisation simulations.

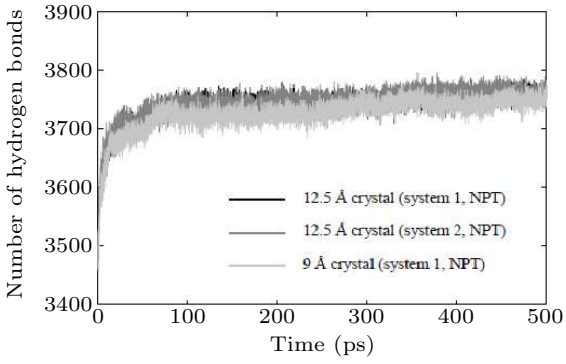


Fig. 7. Number of hydrogen bonds for zero-field crystallisation simulations.

For NNPT simulations in external fields with $E_{\rm rms} \leq 0.1$ V/Å, no crystal dissolution was observed during NNPT runs using system 1 as the initial configuration. Further, longer simulations were performed below this threshold, and dissociation was not observed; since this external-field force is only a few percent of the intrinsic forces experienced in clathrates, this is understandable in terms of a reduced ability to disrupt the hydrate cages (i.e., much smaller than the forces of hydrogen bonds). To test this threshold level *per se*, simulations were also conducted at 0.12 V/Å, and it was found that this exceeded the threshold, i.e., dissociation did occur. In Figs. 8 and 9, the sizes of the hydrate cluster as a function of time are presented in terms of the number of enclathrated water molecules, along with the corresponding zero-field data. Corresponding regression lines during the first 30 ps of interfacial realignment are shown, with smoothed lines thereafter for low r.m.s. field intensities (0.04 V·nm^{-1} and 0.08 V·nm^{-1}) and for 1 V·nm^{-1}, respectively. Reference to the size–time data in Figs. 8 and 9 shows that the application of these lower-intensity fields (i.e., those with $E_{\rm rms} \leq 0.1$ V/Å) results in less obvious changes in the hydrate-cluster growth characteristics, although subtle effects are present.

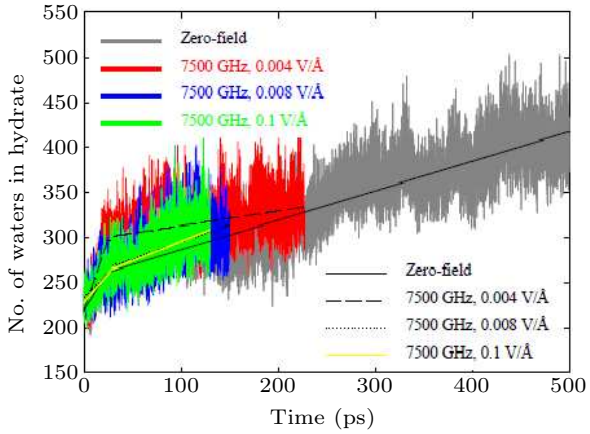


Fig. 8. Hydrate-cluster size as a function of time for system 1 (NNPT) for zero-field conditions and for 7.5 THz fields.

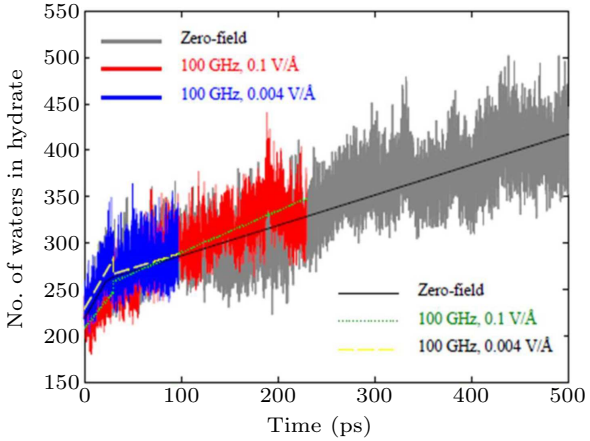


Fig. 9. Hydrate-cluster size as a function of time for system 1 (NNPT) for zero-field conditions and for 100 GHz fields.

It should be noted that the inclusion of regression curves, in some cases, suggests that the growth rate in the presence of certain fields is actually enhanced vis-à-vis zero-field formation, although this was not found to be statistically significant according to student's t-tests. The increased diffusivity of water and methane molecules in e/m fields[15] may result in easier liquid-phase orientational and interfacial relaxation, facilitating enhanced interfacial molecular mass transfer without compromising the cage stability in the crystallites

at lower-intensity e/m fields. It appears that weaker fields do not exert sufficient rotational force on the water molecules to significantly disrupt the hydrogen-bonding network in the nano-crystallite cages, based on the experience of pure liquid water NNPT simulations;[15] r.m.s. field strengths of about 0.5 V·nm^{-1} were required at 298 K before any significant acceleration in hydrogen-bond kinetics and molecular mobility was observed.[15]

In this case, however, the system is non-equilibrium and two-phase, at the lower temperature of 220 K and higher pressure of 600 bar. Therefore, the 'cut-off' field intensity above which the stronger hydrogen-bond network in the clathrate phase would be sufficiently disrupted to bring about dissolution within the simulation timescale would be expected to be higher than 0.5 V·nm^{-1}. We have used velocity randomisation to supplement two additional runs in selected in-field simulations. Table 3 shows the uncertainties in the slope of the growth-rate fits.

Table 3. Selected growth rates uncertainties of post-transient regression-fit slopes (in % of rate).

100 GHz, 0.1 V/A	12.3
100 GHz, 0.004 V/A	17.4
7500 GHz, 0.1 V/A	21.2

In Figs. 10 and 11, hydrate clusters at different phases of the simulations with 0.1 V/Å fields present at 100 GHz and 1000 GHz, respectively, are shown in a series of snapshots. It was found that the newly attached hydrate structures were deformed to some extent relative to the original nanocrystal cluster, in a manner analogous to zero-field growth (cf. Fig. 3). To assess the geometrical shape of the growing hydrate cluster and to investigate any possible anisotropy in the growth process, the aspect ratios of the hydrate crystal were calculated. These were defined as the ratios of the maximum 'diameters', i.e., the distances between the most 'positive' and 'negative' coordinate components of crystal-phase molecules in the x, y, and z directions.

The z/x, z/y, and x/y ratios for the two runs in the presence of the 0.1 V/Å fields at 100 GHz and 1000 GHz are presented in Figs. 12 and 13, respectively, along with the zero-field results for system 1. Such a definition obviously results in considerable statistical scatter: the ratios fluctuate significantly about unity, due to the magnitude of instantaneous phase-classification oscillations at the interface being of the order of a water-molecule diameter (e.g., about 3 Å), which constitutes a substantial fraction of the cluster diameter (i.e., *circa* 25–30 Å). Nevertheless, it appears that the in-field ratios are enhanced vis-à-vis the zero-field cases, showing some level of elongation and anisotropy for "directed crystallisation" in the 0.1 V/Å fields. Two slightly longer in-field simulations were run up to 250 ps for selected intensities and frequencies, and it was found that the fits did not change significantly, so that the original conclusions remain largely unchanged.

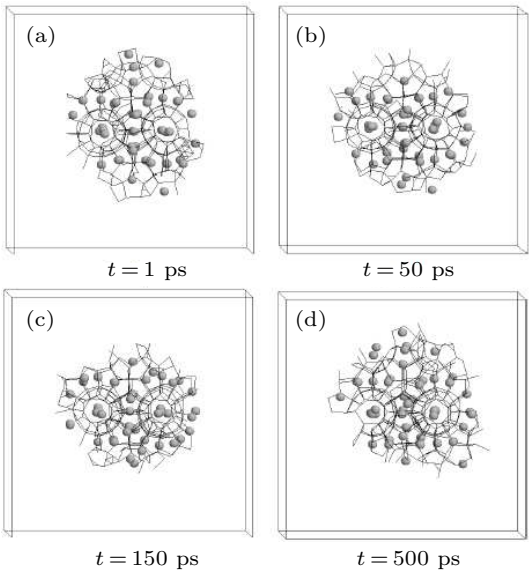


Fig. 10. Snapshots of the cluster configurations for system 1 in the NNPT ensemble, in the presence of a field of 100 GHz/0.1 V/Å.

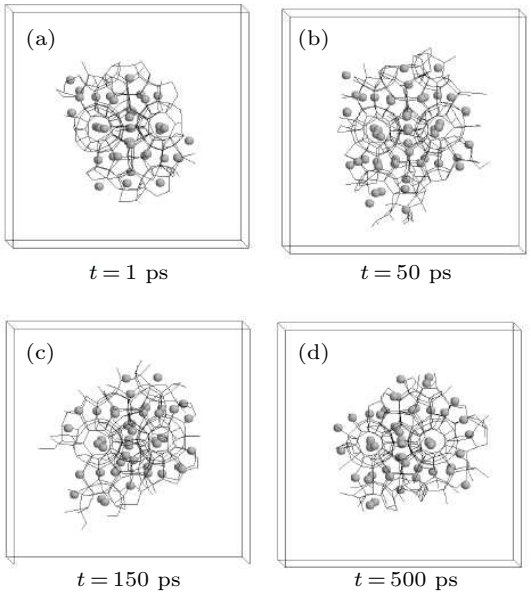


Fig. 11. Snapshots of the cluster configurations for system 1 in the NNPT ensemble, in the presence of a field of 1000 GHz/0.1 V/Å.

Site-site PDFs are depicted in Figs. 14 and 15 for the water–water interactions at various stages throughout the crystallisation of system 1 in the 100 GHz/1 V·nm^{-1} field. The PDFs were sampled over three-period windows. The reported times of 2, 6, and 58 ps roughly align with the centers of specific sampling periods (refer to Figs. 14 and 15), allowing easier comparison with the zero-field PDF results obtained at comparable times (refer to Fig. 4).

It is evident that, at a particular simulation time, the peak structure of the PDFs is less prominent when the 100 GHz/0.1 V/Å field is present. This indicates an effect

of the field on the hydrogen-bonding structure of the water molecules: hydrogen bonding is slightly disrupted, predominantly in the liquid phase, but not sufficiently to disturb the hydrogen-bonding network in the crystal phase (at least over the timescale of the simulation). No significant changes were observed for $E_{\rm rms} \leq 0.1$ V/Å. In the case of the 1000 GHz/0.1 V/Å field, which has the same RMS intensity as the 100 GHz/0.1 V/Å field, the frequency of the applied field (corresponding to a period of 1 ps) appears to be too high to allow the dipoles of the water molecules sufficient time to rotate fully in response to the field, thus having no real effect on the structure in the surrounding liquid. No significant effects on the water-methane or methane-methane PDFs were observed.

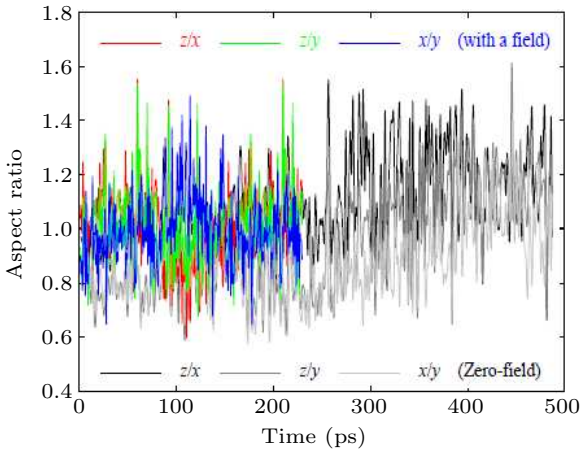


Fig. 12. Hydrate aspect ratios as a function of time for system 1 (NNPT) for zerofield conditions and for a 100 GHz/0.1 V/Å field.

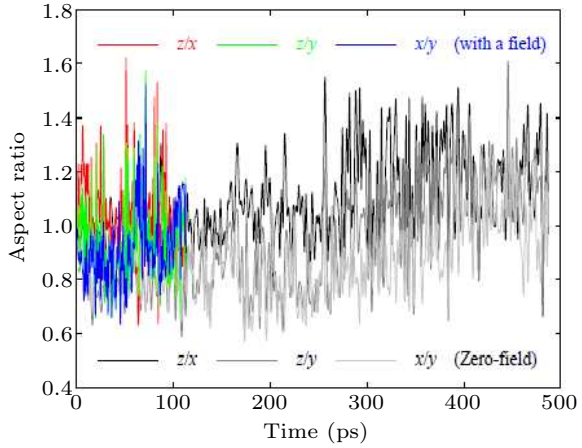


Fig. 13. Hydrate aspect ratios as a function of time for system 1 (NNPT) for zerofield conditions and for a 1000 GHz/0.1 V/Å field.

The main field effects on the energetic stabilization of the system were manifested primarily in the water–water interactions. The 100 GHz/0.1 V/Å field resulted in an average increase in the water–water potential energy by 0.4 kcal/mol, whilst the 1000 GHz/0.1 V/Å field led to an increase of about 0.15 kcal/mol. The potential energy of the applied electric field, $U_E(t)$, is given by

$$U_E(t) = -\boldsymbol{M} \cdot \boldsymbol{E}(t) = -M_z E(t), \tag{4}$$

where $\boldsymbol{M}$ is the total dipole moment vector of the system. This explains the periodic oscillations in the water–water (and total system) potential energy for the 100 GHz/0.1 V/Å field, with a period of 10 ps. In the case of the 1000 GHz/0.1 V/Å field, the period of 1 ps was insufficient to allow appreciable rotational alignment of the water molecules, resulting in less increase in potential energy. Little change was observed in the water–methane and methane–methane potential energy components in the presence of the fields. No significant changes in the energy stabilization characteristics were observed for weaker fields. A decline in the average molecular dipole moment of about 0.03 D (less than 1%) relative to the zero-field value (cf. Fig. 6) was noted, while the 1000 GHz/0.1 V/Å field had no appreciable effect. Fields with $E_{\rm rms} < 0.1$ V/Å did not alter the system or molecular dipole moments.

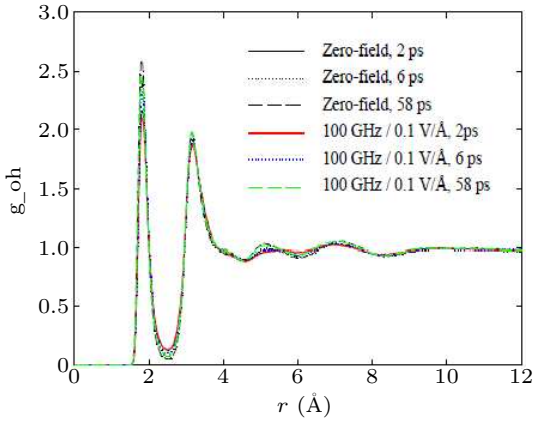


Fig. 14. Oxygen-hydrogen PDF between water molecules at various stages of NNPT crystallisation for system 1 under zero-field conditions and for a 100 GHz/0.1 V/Å field.

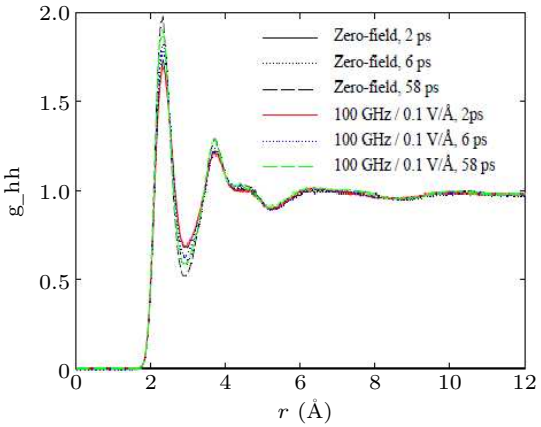


Fig. 15. Hydrogen-hydrogen PDF between water molecules at various stages of NNPT crystallisation for system 1 under zero-field conditions and for a 100 GHz/0.1 V/Å field.

The number of hydrogen bonds decreased by approximately 100 in the 100 GHz/0.1 V/Å field, i.e., a reduction of less than 3% relative to the zero-field value, subject to oscillations commensurate with the field periodicity (10 ps) with amplitude of about 30–40. Since the number of molecules in the clathrate phase is very similar for the zero-field and 100 GHz/0.1 V/Å cases, and the hydrogen bonding in the

hydrate phase is highly regular, the decrease occurs primarily in the liquid phase. This reduction arises from continual rotational realignment of water molecules in the liquid phase, which temporarily breaks additional hydrogen bonds; the periodicity in the number of hydrogen bonds reflects the oscillations in the instantaneous electric field intensity, and hence the rotational force on the water molecules. The 1000 GHz/0.1 V/Å field led to a decline of about 50 hydrogen bonds, but with less pronounced oscillations. No changes in the progression of hydrogen bonds were observed for lower-intensity fields.

4. Conclusions

For hydrate nano-crystallites, ~ 1 V·nm^{-1} appears to induce the onset of e/m-shifted crystallisation, with little appreciable effect observed for lower-intensity fields relative to the zero-field case. A systematic frequency dependence of water-dipole alignment with the external field was observed, providing a mechanistic rationale for dipole direction/magnitude and hydrogen-bonding shifts. Ref. [15] established that e/m fields slightly above this intensity (approaching 1.5 V·nm^{-1}) typically lead to hydrate "electro-dissociation" within timescales of nanoseconds, with similar values for externally applied static electric fields.[17,18]

Importantly, a polarisable water model was employed to represent the response of water molecules to externally applied e/m fields, allowing near-instantaneous electron-density rearrangement and fluctuations to be modeled rigorously (e.g., for sub-picosecond Terahertz frequencies) within the Born–Oppenheimer approximation, as the electronic ground state is considered.

Naturally, e/m-field-controlled crystallisation is expected to have many technological benefits, for example in semiconductor manufacture and polymorph control.[15]

Acknowledgment

The author thanks J.M.D. MacElroy for interesting conversations and technical assistance.

References

[1] Makogon Y F 1997 *Hydrates of Hydrocarbons* (Tulsa:PennWell Books)
[2] Sloan E D and Koh C A 2017 *Clathrate Hydrates of Natural Gases*, 3rd Ed. (Boca Raton: CRC Press)
[3] MacDonald G J 1990 *Annu. Rev. Energy* **15** 53
[4] Kvenvolden K A 1988 *Chem. Geol.* **71** 41
[5] Brewer P G, Orr F M, Friederich G, Kvenvolden K A and Orange D L 1998 *Energy Fuels* **12** 183
[6] Tung Y T, Chen L J, Chen Y P and Lin S T 2011 *J. Phys. Chem. B* **115** 15295
[7] Tse J S, Klein M L and McDonald I R 1983 *J. Phys. Chem.* **87** 4198
[8] Tse J S, Klein M L and McDonald I R 1984 *J. Chem. Phys.* **81** 6146
[9] Tse J S, McKinnon W R and Marchi M 1987 *J. Phys. Chem.* **91** 4188
[10] Chialvo A A, Houssa M and Cummings P T 2002 *J. Phys. Chem. B* **106** 442
[11] Tse J S, Shpakov V P, Murashov V P and Belosludov V R 1997 *J. Chem. Phys.* **107** 9271
[12] Tse J S, Shpakov V P, Belosludov V R, Trouw F, Handa Y P and Press W 2001 *Europhys. Lett.* **54** 354
[13] English N J and Clarke E T 2013 *J. Chem. Phys.* **139** 094701
[14] Rojey A 1997 U.S. Patent No. 5625178
[15] English N J and MacElroy J M D 2004 *J. Chem. Phys.* **120** 10247
[16] Waldron C J and English N J 2017 *J. Chem. Phys.* **147** 024506
[17] Luis D P, López-Lemus J and Mayorga M 2010 *Mol. Simul.* **36** 461
[18] Luis D P, Herrera-Hernández E C and Saint-Martin H 2015 *J. Chem. Phys.* **143** 204503
[19] Waldron C J and English N J 2016 *Chem. Phys. Lett.* **649** 119
[20] Rick S W, Stuart S J and Berne B J 1994 *J. Chem. Phys.* **101** 6141
[21] Lekner J 1989 *Physica A* **157** 826
[22] Lekner J 1991 *Physica A* **176** 485
[23] Grønbech-Jensen N 1997 *Int. J. Mod. Phys.* **8** 1287
[24] Allen M P and Tildesley D J 2017 *Computer Simulation of Liquids*, 2nd Ed. (Oxford : Oxford University Press)
[25] Asfar M N and Hasted J B 1977 *J. Opt. Soc. Am.* **67** 902
[26] Zelsmann H R 1995 *J. Mol. Struct.* **350** 95
[27] Bertie J E and Jacobs S M 1977 *Can. J. Chem.* **55** 1777
[28] Bertie J E and Jacobs S M 1982 *J. Chem. Phys.* **77** 3230
[29] English N J 2005 *Molec. Phys.* **103** 1945
[30] English N J and MacElroy J M D 2002 *Molec. Phys.* **100** 3753